Electrochemical performance evaluation of a Ni/Fe mixed oxide natural clay composite as anode material for Li-ion batteries

Augusto Rodríguez , Mariela Ortiz , Jorge Thomas , Arnaldo Visintin

PII: S0013-4686(24)00113-0
DOI: https://doi.org/10.1016/j.electacta.2024.143869
Reference: EA 143869

To appear in: *Electrochimica Acta*

Received date: 21 July 2023
Revised date: 7 December 2023
Accepted date: 21 January 2024

Please cite this article as: Augusto Rodríguez , Mariela Ortiz , Jorge Thomas , Arnaldo Visintin , Electrochemical performance evaluation of a Ni/Fe mixed oxide natural clay composite as anode material for Li-ion batteries, *Electrochimica Acta* (2024), doi: https://doi.org/10.1016/j.electacta.2024.143869

Electrochemical performance evaluation of a Ni/Fe mixed oxide natural clay composite as anode material for Li-ion batteries

Augusto Rodríguez[1,4], Mariela Ortiz[2], Jorge Thomas[3] and Arnaldo Visintin[1]

[1]Instituto de Investigaciones Fisicoquímicas Teóricas y Aplicadas (INIFTA), Facultad de Ciencias Exactas (UNLP), CONICET, Diag. 113 y 64, B1900 La Plata, Argentina.

[2]Centro de Investigación y Desarrollo en Ciencia y Tecnología de Materiales (CITEMA), Universidad Tecnológica Nacional - CICPBA, 60 y 124, 1923, Berisso, Argentina.

[3]YPF Tecnología S.A., Av. del Petróleo Argentino S/N (129 and 143), B1923 Berisso, Buenos Aires, Argentina.

[4]Author to whom any correspondence should be addressed: augustorodriguezarg1992@gmail.com

Abstract

A Ni/Fe mixed oxide natural clay composite was obtained by simple addition of bentonite natural clay sample after coprecipitation of layered double hydroxide ($Ni_{0.75}Fe_{0.25}(OH)_2(CO_3)_{0.125}$) precursor; later this composite was sintered at 400 °C. The natural clay was collected from La Plata city (Argentina), and this has been used without further purification treatment. The electrochemical characterization allowed to identify stability improvement of the charge-discharge capacity values for the materials with calcination (35% capacity retention after 60 cycles) against an anode prepared without clay (only 8% retention). However, the anodic material without clay delivered a higher discharge capacity than the anode material with clay, as expected, due to the lacking the non-electroactive clay quantity. Physical characterization of the materials, such as nitrogen physisorption, showed a smaller particle diameter (37 nm against 54 nm) for the mixed oxides with and without natural clay, respectively. Despite this, by scanning electron microscopy a greater size difference was observed in the morphology for the oxide- natural clay composites. This could be because the smaller

particle size along the interstitial space of the consecutive clay flakes and the pore volume of the material could be produced a synergistic effect between them; and thus promote a buffered volumetric expansion. This is generally reported to be responsible for the low charge- discharge cyclic performance observed in the conversion anodes. Also, the process of re-dissolution of the hydroxide precursor in the basic media, followed by the double hydroxide re-precipitation from Ni^{+2} and Fe^{+3} which are adsorbed in negative sites of the clay could be responsible for the achievement of the smaller size particles.

Keywords: Lithium-ion battery, Anode, Natural clay mineral, Ni/Fe oxide, Layered double hydroxide.

1. Introduction

While the development of new lithium-based energy storage systems, such as, Lithium-Sulfur and Lithium-Air, are still not achieving the requirements for their massive commercial application [1-3]. Research over new materials for Li-ion battery systems keeps producing new advanced compounds and methods along their related to numerous scientific studies [4]. Most efforts have been focused on developing new cathode materials [5], mainly due to the fact, that the commercial graphite anodes, with their low cost and relatively high discharge capacity (372 mAh g^{-1}) [6] can be used for manufacturing commercial Li-ion batteries. The cathode materials used have lower discharge capacity values than those for anodic materials; being the cathode the electrode that limits the overall discharge capacity of the electrochemical cell.

The new cathode materials are progressively delivering higher capacities than commercial materials [7-8]. So, the graphite could be replaced, in the full cell configurations, by new types of electroactive compounds, such as, Ni, Fe, Mn, Cu and Co oxides [9] (between these the Co should be avoided due its high cost and toxicity [10]). These oxides present initial capacities easily above 500 mAh g^{-1} [11], [12]. Nonetheless, their rapid capacity fade is an important phenomenon that still prevents its use in

commercial technologies [13]. Several attempts have been made suppress the poor cyclability observed of the materials by superficial and structural modifications. However, this involves more consecutive steps in material synthesis processes [12] which could difficult their industrial scalability.

Ni/Fe mixed oxides usually report initial capacities above 1000 mAh g^{-1} [14], since 2 and 3 Li^{+} ions can react by each Ni and Fe cation, respectively. But, in order to obtain good cyclability, different reaction processes, such as hydrothermal methods [14], are required or the incorporation of porous matrices which might present higher costs [14]. In this study, we present the evaluation of a Ni/Fe mixed oxide obtained through partial calcination of coprecipitated layered synthetic clay (hydrotalcite) as anode material, and its electrochemical performance when a natural clay mixture sample is added to the reaction media. Clay materials are known for their high levels of porosity, high surface areas, abundance, and low cost [15]. Therefore, they are excellent candidates as catalytic or non-catalytic supports according to their chemical composition [15]. The clays generally are composed essentially of consecutives sheets of SiO_4 tetrahedral stacked between sheets of octahedral AlO_6, where Al^{+3} can be replaced by Fe, Mg, Mn, etc. and the oxygen can also be found in the form of OH^{-} [16]. Aluminum substitution gives rise to the presence of permanent charges [17] that are stabilized by the intercalation of cation such as Na^{+}, K^{+}, Ca^{2+} and Li^{+}.

Layered double hydroxides, or, also known as hydrotalcite clays, correspond to a family of layered compounds of general formula $M^{II}_{1-X}M_X^{III}(OH)_2(A^{N-})_{X/N}$ [18]. Composed entirely by stacked octahedral sheets of $M^{II}O_6$ and $M^{III}O_6$ where M^{II} can be Mg^{+2}, Ni^{+2}, Co^{+2}, etc. while M^{III} is Al^{+3}, Fe^{+3} or other trivalent transition metal. Charge disbalance between M^{II} and M^{III} produces a partial positive charge that is compensated by interlayer anions (A^{N-}) [18]. The use of hydrotalcites or other Si/Al natural clays as cation and anion exchangers has been extensively reported [19-20], as well as the catalytic properties of sintered layered double hydroxides [21]. However, there are few studies of sintered layered double hydroxides/natural Si/Al clay mixtures used as active material of lithium-ion

battery anodes, but further research is needed to understand the interactions of these structures with Li^+ and improve their electrochemical performance as anode material.

2. Experimental

2.1. Natural clay sample selection (NC)

The natural clay sample was collected from peripheral areas to the La Plata city (Argentina). The selection of the clay mineral sample was based on its malleability in the presence of water and the visible shrinkage behavior when it was dry. The sample was free from coarse materials from origin; However, the clay was sieved through a 350 μm mesh and later pulverized in a planetary ball miller for 30 minutes with 3 mm stainless steels spheres. The resulting powders were dried at 96 ºC for 12 hours. Purification steps were not included due to the small amount of natural clay that would be added.

2.2. Synthesis of the hydrotalcite precursor $Ni_{0.75}Fe_{0.25}(OH)_2(CO_3)_{0.125}$ (HT)

The layered double hydroxide was obtained by the co-precipitation method reported by Miyata [22] with some modifications: 200 mL solution of concentrations 0.137 mol/L of $Ni(NO_3)_2.6H_2O$ and 0.046 mol/L of $Fe(NO_3)_3.9H_2O$ (Anedra) was prepared; then 200 mL of a solution containing 0.62 mol/L g of NaOH (Mallinckrodt) (2.07 g in excess for the required co-precipitation) was added dropwise under constant magnetic stirring until completing the hydroxide precipitation. Then, 3 g of Na_2CO_3 (Merck) were added to the reaction media in order to exchange the interlaminar NO_3^- for CO_3^{2-}. The mixture was stirred for 30 minutes and then heated to 50 ºC for 30 minutes. The solids were filtered, then these were washed with deionized water and dried at 96 ºC for 12 hours.

2.2.1. Synthesis of the hydrotalcite precursor $Ni_{0.75}Fe_{0.25}(OH)_2(CO_3)_{0.125}$ + Natural clay (HT2NC)

Another sample was synthesized under similar conditions to those described in the previous section (2.2), but with a modification: after the NaOH and Na_2CO_3 addition 2.0 % w/w of the natural clay sample was added.

2.2.2. Synthesis of the mixed oxides anode materials

The obtained materials (HT and HT2NC) were sintered at 400 ºC during 4 hours under air atmosphere (ESTIGIA oven) obtaining the corresponding oxides labeled as HT-400 and HT2NC-400.

2.3. Physical and chemical characterization of the materials

The crystallographic structures for the four samples (NC, HT, HT-400 and HT2NC-400) were identified by X-ray diffraction in a Philips-APD PW 1710 diffractometer with Cu Kα (1.542 Å) radiation in the range between 5 and 80° (2θ), with a step of 0.02° and a time step of 0.5 seconds/step, and cell parameters where quantified by means of the Rietveld method. Functional group characterization was carried out by Fourier transform infrared (FTIR) spectroscopy with a Thermo Scientific Nicolet iS5 equipment, using an attenuated total reflectance (ATR) accessory with a diamond window, in the wavenumber range 400–4000 cm^{-1} at room temperature. Scanning electron microscopy (SEM) and energy dispersive spectroscopy (EDS) were performed with FEI Quanta 200 ESEM scanning electron microscope. Thermogravimetric analysis was performed in an TGA Q500 equipment (Temperature ramp: 5.00 °C min^{-1}, from ambient temperature to 800 °C and under air atmosphere). Also, N_2 adsorption isotherm profiles were achieved through ASAP2020 equipment.

2.4. Electrochemical characterization

The working electrodes were made by preparing slurries with the following mass fraction: 80% of the electroactive mixed oxides (HT-400 and HT2NC-400), 10% of conductive Super P carbon, and 10% of polyvinylidene fluoride (PVDF) dissolved in N-methyl-2-pyrrolidone (NMP). The suspension was coated on copper foil and was dried at 80 °C until the NMP evaporation. Then, 12-mm diameter electrodes were cut. The electrochemical experiments were performed in Swagelok T

cells, assembled inside M-Braun argon-filled love box. Lithium foil was used as counter and reference electrodes. A glass microfiber membrane was used as separators, and 1 M solution of lithium hexafluorophosphate ($LiPF_6$) dissolved in a 1:1 w/w mixture of ethylene carbonate (EC) and dimethyl carbonate (DMC) as the electrolyte. Cyclic voltammetry (CV) was measured by Gamry Reference 3000 potentiostat, with scan rate of 0.1 mV s^{-1} in 3-0.01 V potential range. Electrochemical impedance spectroscopy (EIS) was performed using Gamry Reference 3000 potentiostat in the frequency range of 100 kHz to 1 mHz. Galvanostatic charge–discharge cycling was carried out on the Arbin multichannel potentiostat/galvanostat (MSTAT4) in the potential range of 3-0.01 V vs. Li^+ /Li, at different current densities (C rates, which was estimated from the charge calculation from the cyclic voltammetry).

3. Results

3.1. DRX analysis

The obtained DRX pattern for the natural clay sample is shown in Figure 1, where the predominant signals that can be observed correspond to those related to a montmorillonite clay type of bentonite sample, along with quartz and some feldspars [23], [24], [25]. Other signals correspond to unidentified impurities for this sample. The plane (001) is related to the c value in the unit cell [26] and its location depends on the chemical species located in the interlaminar space such as water molecules and cations. The broadness of this peak is characteristic of this types of clay and indicates the heterogeneous distribution of hydration states [26] as well as the heterogeneous distributions of cations.

The set of signals expected for a layered double hydroxide is well reported, for the pristine hydrotalcite (Figure 2) a set of peaks located at 11.48 º, 22.93 º, 33.44 º are assigned to diffraction from the (003), (006) and (009) planes, respectively [18]. The last peak overlaps with the plane (012), which is a signal related to turbostratic disorder among the stacked layers [27]. The plane (015) is

result by the same phenomena, while the reflection (110) close to 60 º is representing the distance between the metallic cations inside the octahedral sheets [28]. The intense (003) basal plane signal can be used to determine the interlayer space between the brucite-like sheets by means of the Bragg's equation. This distance corresponds to 7.67 Å for the obtained material, which correlates well with the reported value when carbonate anions are located in the interlayer space [29]. After calcination of both samples (with and without natural clay) an important level of crystallinity is lost, which can be seen by the broadening of the signals and their intensity fade, the (006) plane can no longer be observed. However, the presence of the (003) plane still indicates an important remnant of the layered phase; which, after calcination shows a displacement to higher 2ϴ degrees, demonstrating a decrease in the interlayer space due to the loss of the carbonates anions (7.67 Å to 6.50 Å). Additionally, three symmetric peaks appear at 36.98 °, 43.17 ° and 62.70 ° that correspond to the formation of the Ni(Fe)O_X solid solution with the planes (111), (200), and (220) [30]. Also, signals related to the formation of the phase $NiFe_2O_4$ was not observed at the selected temperature treatment [30], neither signals from the clay mineral were observed, this is due to the low amount used.

Table 1. Lattice parameters of the samples obtained by Rietveld refinement

Lattice Parameters	HT	HT-400$_{(a)}$	HT2NC-400$_{(a)}$
a (Å)	3.093(3)	4.17(2)	4.15(4)
b (Å)	3.093(3)	4.17(2)	4.15(4)
c (Å)	23.044(3)	4.17(2)	4.15(4)

(a) The presented parameters correspond to the solid solution Ni(Fe)O_x using NiO space group as reference

Table 1 shows the obtained cell parameters for the samples. The HT material displays a and c values with good agreement to those reported to CO_3 Ni_3Fe hydrotalcites [30]. However, with a small deviation toward a lowers magnitude that could indicate a Fe^{+3} concentration slightly higher than expected [30]. For the lattice parameter determination of the calcined samples, the NiO space group was used as template for the evaluation of the solid solution phase Ni(Fe)O_x [30]. For a, stoichiometric

Ni/Fe mixed oxide the NiO cell parameter (4.1684(1) Å [31]) would be expected to decrease due to the incorporation of smaller ionic radius Fe^{+3}. However, the obtained parameter for the *HT-400* sample indicates a small increase in the unit cell, this could be the result from the excess of oxygen incorporated at low temperature (400 ºC) which is a characteristic of the synthesis conditions for non-stoichiometric NiO oxides [32]. The HT2NC-400 shows a small decrease in the unit cell parameters as should happen by the Fe^{+3} incorporation [30], which could be because these sample present a more stoichiometric composition for the mixed oxide phase (Rietveld refinement for the composite is presented in figure 2.b).

3.2. FTIR characterization

The FTIR spectra for the natural clay can be observed in figure 3, where a high level agreement between the obtained bands with those reported for bentonite clay is obvious upon simple inspection [33]. The band assignments are: bands located at 3400 and 1638 cm^{-1} correspond to –OH stretching and bending respectively from adsorbed water; 3617 cm^{-1} band represents the –OH stretching from the clay structure; 1118 cm^{-1} and 991 cm^{-1} are the Si-O stretching out of plane and stretching in plane vibration, while the 914 cm^{-1} signal is the AlAlOH bending [34-35]. The almost imperceptible band located at 1420 cm^{-1} can be assigned to vibration from CO_3^{2-} present in the sample [36]. Following with the low frequency region the 516 and 465 cm^{-1} bands are attributable to Si-O-Al and Al-OH vibration respectively. 682 cm^{-1} is a vibration related to quartz and the 772 cm^{-1} is also possibly related to SiO_2 vibration but in the form of tridymite [34-35]. It is important to note that intense signals located at 2900-2800 cm^{-1} where not observed, which shows the absence of C-H bonds as evidence from the lack of important quantities of common organic impurities such as humic and fulvic acids [37]

Figure 4 shows the corresponding spectra for the layered double hydroxide and clay mixture before and after calcination at 400 °C; in both steps, the observable signals correspond to the hydrotalcite compound and its reactions during calcination. The signals related to the low quantity (2% w/w) of

the natural clay additive there are not identified. Before sintering process, the broad band located at 3457 cm^{-1} and the low intensity bands at 1641 cm^{-1} are assigned to the double hydroxide (brucite layers) and adsorbed water –OH stretching vibration and bending vibration, respectively [16]. The medium intensity band located in 1362 cm^{-1} related to the (*v3*) vibrations of the interlaminar CO_3^{2-} [38]; while the 614 cm^{-1} band could be related to the vibration mode (*v*4) of the same anion [38]. The rapid decrease in transmittance at wavenumbers smaller than 500 cm^{-1} is usually related to the undefined signals from the bonds O-M-O [18]. The broad shoulder, at 2985 cm^{-1}, can change its location according to the composition and the interlaminar anion. However, this is related to hydrogen bonding between interlaminar H_2O and the anions [39]. After calcination, as expected, all the signal related to the interlayer CO_3^{2-} show an important decrease in transmittance due to the partial decarboxylation, as well as the partial dehydroxylation and dehydration that lead to a decrease in the –OH vibration modes signals [29].

3.3. Thermogravimetric analysis

Figure 5 shows the thermogravimetric analysis for both samples: the natural bentonite clay and the synthesized Ni/Fe layered double hydroxide. The bentonite clay material presents an important weight loss centered at 50 °C (in a range comprising 23-190 °C) that correspond to the loss of water molecules (from the surface as well as interlayer water) [40]. The low intensity weight loss located at 613 °C can be assigned to dehydroxylation of the structure [41] as well as the decomposition at 442 °C that can also be related to the same process [42]. The overall shape of the TG profile correlates to those reported elsewhere [42]. Additionally, the total weight loss of the clay (~10 %) shows similarity to the total 10.75% loss of reported Na-montmorillonite [42]. The resulting profile for the Ni/Fe layered double hydroxide shows 4 main decomposition steps (at 52, 163, 263 and 444 ° C); which are related to the removal of water molecules from the surface of the materials, the removal of water from the interlayer space in interaction with carbonate anion, dehydroxylation and carbonate decomposition close to 290 °C and also, the total removal of carbonates and hydroxyl groups

respectively [30], [43]. According to these results, the selected calcination temperature (°C) would allow the presence of carbonates and hydroxyl groups, as was observed by FTIR characterization.

3.4. Textural properties

Figure 6 shows the Nitrogen adsorption/desorption isotherm of the raw bentonite sample. A hysteresis loop (H3 Type [44]) indicates the presence of mesopores after the adsorption process, while the overall shape of the profile indicates a type IV isotherm according to the IUPAC classification [45]. The BET specific surface area (72 $m^2 g^{-1}$) shows good correlation with those previously reported for bentonites [46].

Also, Isotherms are classified as type IV with an H3 hysteresis loop for the calcined modified and unmodified layered double hydroxide (Figure 7 [47]). The BET results exhibit specific surface areas of 111 and 160 $m^2 g^{-1}$ for HT-400 and HT2NC-400 samples, respectively. Table 2 presents the values of the specific areas, pore volumes, pore diameters and average particle sizes of the synthesized materials.

Table 2. Textural properties

	BET Surface ($m^2 g^{-1}$)	Pore volume $(cm^3 g^{-1})_{(a)}$	Pore diameter $(nm)_{(a)}$	Average particle size (nm)
NC	72	0.05768	4.78	83
HT-400	111	0.2504	7.88	54
HT2NC-400	160	0.2416	5.22	37

(a) BJH Method

From the table 2, it can be seen that the raw bentonite sample has the lowest BET surface area. However, its addition to the synthesis process for HT leads to a smaller particle size and higher surface areas after calcination, while the pore volume presents only a small decrease from 0.25-0.24 $cm^3 g^{-1}$. It is reported [48], that bentonite clay materials may present an increase to their maximum surface areas after calcination at 400 °C. In order to evaluate this contribution, a sample bentonite clay sample

was treated in alkaline media (0.500 g of sample were put inside 100 mL solution with 2.07 g NaOH) and then these were calcined at 400 °C of temperature without the presence of the Ni and Fe layered double hydroxide. So, this blank sample was analyzed to examination only the changes that the clay may present in the media and procedure like the synthesis for HT materials. The isotherm of the alkaline-treated and sintered clay (data not shown) has a lower BET surface (65 $m^2 g^{-1}$), which verifies that the phenomena of structural modification of the clay portion (2 %) during calcination is not responsible of the increase in area of the total composite HT2NC-400.

Taking into consideration the following three aspects: (i) Ni^{+2} and Fe^{+3} are cations that can be well adsorbed inside bentonites/montmorillonite clays [49]; (ii) Ni/Fe HT must present some precipitation equilibria, especially with the small re dissolution due the formation of $Fe(OH)_4^-$ and $Ni(OH)_4^{2-}$ species in alkaline media [50-51]; (iii) the clay presents pH dependent negative sites in the presence of OH^- due to deprotonation of the outer surface of the clay [52]. A HT redissolution- precipitation process over the clay could be responsible for the smaller obtained particles (Figure 8). HT suffers a partial dynamic redissolution in the alkaline media, so the cations are adsorbed in negative sites of the clay resulting from the high pH value. So, the precipitation is a dynamic process the adsorbed cations give origin to nano particles of the HT over the clay, which decrease their size even more during calcination.

3.5. Scanning electron microscopy and EDS

Table 3. Estimated qualitative composition of the clay sample from EDS analysis

Formula	**SiO_2**	**Al_2O_3**	**MgO**	**Fe_2O_3**	**Na_2O**	**CaO**	**K_2O**	**TiO_2**
Composition (%)	60.70	20.22	2.19	9.05	1.24	2.08	3.48	1.02

Figure 9 shows the SEM image obtained for the natural ray clay under high magnification, where an agglomerate of flake-like particles can be observed. This morphology is typically reported for clay materials including for bentonite/montmorillonites [53-54]. Any other type of crystalline

agglomerates related to other materials were not observed. The EDS elemental distribution (figure 10) exhibits a homogenous distribution of the main elements of the material, while the estimated composition presented in their respective oxides, in order to easily compare with the available informed compositions. [55] The values of table 3 present an acceptable agreement with some of the reported ranges for each element [55]. The EDS analysis did not show the presence of Ni atom in the natural clay, neither it was expected [55] since is not common to find Ni in typical bentonite-type clays.

Figure 11 shows the obtained SEM images for the layered double hydroxide precursor (a) and the respective sintered materials, without (b) and with the added natural clay (c). The precursor shows heterogeneous distribution of particles with some smaller flake-like portion that resemble the hydrotalcites morphology [56]. After calcination (Fig. 11.c), a more heterogeneous particle size distribution can be observed for the samples without the clay while for the clay-modified oxide an agglomerate of smaller rounded particles can be observed by simple inspection.

The figure 12 shows the SEM images for the modified and unmodified materials with their EDS elemental distribution. From the low amplification images, it can be seen how the unmodified sample is a set of large size agglomerates. In contrast, the clay-modified oxide (HT2NC-400) presents particles with a wide distribution of sizes. Both materials exhibit a uniform distribution of Ni and Fe, with the inclusion of Si and Al distribution for the modified oxide, which, for the raw natural state of the clay, shows some zones with higher Si and Al concentration.

3.6. Cycling performance

Figure 13 shows the galvanostatic cycling performance for the modified and unmodified oxide samples. The unmodified sample exhibits a higher discharge capacity above 800 mAh g^{-1}, which is remained during 10 cycles and later it presents a rapid capacity fade. In contrast, the modified material delivers a lower initial discharge capacity, above 600 mAh g^{-1}. However, the rapid capacity fade is

not observed after 10 cycles leading to a lower capacity decrease rate with an improvement in the cyclability (insert in figure 13). The difference between initial discharge capacity values could be related to the inactive clay portion which was not subtracted during the calculation of the resulting capacities. The overall capacity fade occurs due the low conductivity, volumetric expansion and electrochemical irreversibility in the mechanism of conversion type anodes [13]. The cycling performance of the material was also evaluated in a CCCV protocol (Constant potential at 0.01 V until reaching 5% of the original applied current. Data not shown) where it can be seen that the unmodified materials presents a higher capacity fade compared with the obtained under CC protocol. While, the modified material keeps the same behavior regardless of the implementation of CC or CCCV evaluation. This represent an important characteristic, since the performance in full-cell configuration (battery prototypes) is usually evaluated under CCCV protocols [57]

Figure 14 exhibits the charge-discharge profiles for both materials, in the potential range of 3.0-0.01 V and a C rate of 0.2 C. During the first cycle, capacities above 1000 mAh/g are achieved for both materials, with a well-defined plateau located between 0.50 and 0.70 V vs Li/Li^+ that are in good correlation with the plateaus observed in other NiO or Fe_2O_3 anodes [58-59]. After the second cycle, there is an important shift in the observed potentials due to structural modifications [59], while the plateau is gradually lost due to the expected formation of amorphous $Ni/Fe/Li_2O$ composites after consecutive cycling [13]. However, after 40 cycles the modified material remains a higher capacity than the anode with unmodified samples. In order to evaluate any possible contribution of the clay to the discharge capacities, electrodes with only Super P/Clay and Super P where prepared (insert: figure 14.a) and later studied by cyclic voltammetric technique. The curves result nearly similar, and the signals are most likely corresponded to graphite residues [60] present in the conductive Super P and the Lithium storage in graphene edges [61]. With this, is possible to confirm that the clay mineral, according to small quantities of impurities. Although it has an impact in the morphology of the material: its composition does not contribute directly in any faradaic reaction since no unidentified

peaks where observed related to Si reduction or electrochemical decomposition of any organic contaminant.

3.7. Cyclic voltammetry

The voltammograms, during the first and second cycle, (Figure 15) show good correlation with the available information on the electrochemical behavior of NiO and F_2O_3 oxides. During the first cycle, the sharpness of the reduction peak indicate that both are mesoporous materials [62], for a Fe_2O_3 oxide such peak should be seen at 0.70 V [63], while for NiO the peak should be located at 0.41 V [62]; a single peak located exacted at the middle point was obtained (~0.55 V). This could indicate that the reduction reactions Ni^{+2} to Ni^0 and Fe^{+3} to Fe^0 are both taking place at the same potential with the insertion of Li^+ into the whole structure to form Li_2O as a conversion type anode. For the oxidation signals, a broad low intensity peak at 1.60 and 1.66 V corresponds to the reversible Fe^0 to Fe^{+3} reaction [63] while the 2.25 V signal is assigned to the Ni^0 to Ni^{+2} reaction [62]. Again, the difference in intensity between both electrodes could be due to the presence of the non-electroactive clay. For the second cycle, the potential for each reaction shows a shift, especially for the reduction reactions which is shitted from nearly 0.50 V to ~0.90 V. These is in correlation with the behaviors observed elsewhere [62-63]. All assigned peaks agree with the charge and discharge profiles from figure 14.

After 200 cycles (Figure 16), the intensity of the reduction and oxidations peaks shows an expectable decrease due to irreversibility and volumetric expansions that slowly compromise the structure stability of the materials [13]. Likewise, the discharge capacity of the electrodes has faded to 160 and 53 mAh g^{-1} for the modified and unmodified materials respectively. For the HT2NC-400 electrode the reduction and oxidation peaks are still visible, while the HT-400 electrode present almost just non-faraday contribution. This improvement of the stability presented by the modified material (Ni/Fe mixed oxide and clay), could be due to the reduce size of its particles. Furthermore, even though the modification lead to a very small decrease in pore volume (0.24 cm^3 g^{-1}). This volume becomes

relevant in comparison with the expected volume of the smaller particles; which in time generates a better buffer effect for the volumetric expansion that is responsible for the capacity fade

3.8. Electrochemical impedance spectroscopy (EIS)

Electrochemical impedance spectroscopy was performed in both electrodes after 200 galvanostatic cycles (Figure 17). The high frequency region (insert, figure 17.a) displays a loop related to charge transfer resistance (R_{ct}) [62] for the unmodified material. Two loops can be observed for the modified material, one is assigned to the charge transfer resistance and another, at the highest frequency, is corresponding to the presence of a detectable solid/electrolyte interface (R_{SEI}) [64]. It is known that the presence of a SEI plays a major role in the stability of cathode and anode materials [65] and its occurrence is negatively affected during volumetric expansion since the SEI film could continuously break. once more, these verified the existence of a volumetric buffer effect. Both electrodes show a diffusion tail at low frequencies, where the Warburg constant (Figure 17.b) is much lower for the HT2NC-400 material (70 $\Omega\ s^{-0.5}$ against 740 $\Omega\ s^{-0.5}$). This could indicate a higher diffusion coefficient [66] which could be facilitated for the modified material by a higher Pore Volume/particle size ratio [67] (porosity of the material) The adjustment of the data to the equivalent circuit (insert, Figure 17a) indicates, as expected, a higher R_{SEI} for the modified material against the non-modified one (106.1 against 66.1 Ω respectively). This difference supports the evidence for the better formation of the solid/electrolyte interphase for HT2NC-400 material. Likewise, the modified material presented a higher resistance to the charge transfers due to the presence of the clay (19120 against 6936 Ω).

3.9. Rate Capability

The rate capability for the materials is presented (Figure 18), where high charge and discharge rates up to 10 C-rate were applied in the. Both electrodes restore progressively their discharge capacity values after the last 10 C cycle until reaching similar maximum capacities in percentages with respect to the initial discharge capacity values (~75% of recovery for the two electrodes). Nonetheless, the

non-modified anode (HT-400) despite presenting a higher initial discharge capacity values when applying C-rates of 10 C, the capacity values drop slightly below to those obtained from the modified mixed oxide (23 against 38 mAh g^{-1} respectively). This could indicate a slightly higher capacity fade rate for the non-modified material. The bigger difference can be observed when it was cycling from 2 C to 5 C: the unmodified materials present a 66% loss of capacity vs. 43% for the modified electrode. This drop could be attributed only to the applied C-rate and not to the overall life-cycle-state of the electrode because these remain in their similar values of discharge capacity after the used higher C rates. The lower discharge capacity was observed for both electrodes at first cycle, and these could be corresponding to degree of self-discharge. These phenomena can be identified during a small rest time after performing cyclic voltammetry, which lead to and incomplete charge obtainment in the first cycle of the reported rate-capability

4. Conclusions

Ni and Fe mixed oxides ($Ni(Fe)O_x$ solid solutions with Ni and Fe in the proportion 3:1) were synthesized by calcination of $Ni_{0.75}Fe_{0.25}(OH)_2(CO_3)_{0.125}$ hydrotalcites at 400 ºC during 4 hours. The obtained oxide delivered an initial discharge capacity above 1200 mAh g^{-1} during the first cycle, following a capacity drop to ~870 mAh g^{-1} keeping its stable behavior until cycle 20 where the material losses most of its capacity. The addition of a 2% sample of a natural clay (bentonite) during the precipitation of the hydrotalcite precursor led to the formation of the mixed oxide with smaller particles, and discharge capacity that although is initially lower (~1100 and 600 mAh g^{-1} first and second cycle respectively). This material presents a better cyclability during 60 galvanostatic cycles keeping a constant capacity fade slope. Also, the modified material presents an improvement in the rate-capability of the cathode for higher C-rates (10 C). The results indicate that the improvements could be related to the reduced size particles (particle to pore volume relation), that provides the buffering of the well-expected volumetric expansion in conversion type anodes, allowing the presence of a more stable solid electrolyte interfase and a better Li^+ diffusion to the particles. We suggest that

the smaller particle size is produced thanks to a redissolution and re precipitation process of the hydrotalcite precursor over the functional charged groups of the clay due to the basic media of the synthesis. Although the discharge capacity values are still not stable enough to replace or to be compared with the commercial graphite electrodes. These studies present an easy method to partially improve the cycling performance for this type of materials, which through further investigation, could lead to the achievement of the stabilized of the electrochemical performance during long charge-discharge cycling analysis.

Credit author statement

We confirm that the manuscript has been read and approved by all named authors and that there are not other persons who satisfied the criteria for authorship but are not listed. We further confirm that the order of authors listed in the manuscript has been approved by all of us.

Declaration of Competing Interest

None.

Acknowledgements

Authors would like to acknowledge the financial support provided by the Consejo Nacional de Investigaciones Científicas y Técnicas (CONICET) and the Agencia Nacional de Promoción Científica y Tecnológica (ANPCyT).

References

[1] M. Xiao, Z. Xing, Recent Progress of Lithium-Sulfur Batteries, Batteries 9 (2023) 79. https://doi.org/10.3390/batteries902007

[2] S. Dörfler, H. Althues, P. Härtel, T. Abendroth, B. Schumm, S. Kaskel, Challenges and Key Parameters of Lithium-Sulfur Batteries on Pouch Cell Level, Joule 4 (3) (2020) 539-554. https://doi.org/10.1016/j.joule.2020.02.006

[3] N. Imanishi, O. Yamamoto, Perspectives and challenges of rechargeable lithium–air batteries, Materials Today Advances 4 (2019) 100031. https://doi.org/10.1016/j.mtadv.2019.100031

[4] S. Mahmud, M. Rahman, M, Kamruzzaman, M. Osman Ali, M. Shariful Alam Emon, H. Khatun, M. Ramjan Ali, Recent advances in lithium-ion battery materials for improved electrochemical performance: A review, Results in Engineering 15 (2022) 100472. https://doi.org/10.1016/j.rineng.2022.100472

[5] J. Jyoti, B. P. Singh, S. K. Tripathi, Recent advancements in development of different cathode materials for rechargeable lithium ion batteries, Journal of Energy Storage 43 (2021) 103112. https://doi.org/10.1016/j.est.2021.103112

[6] H. Zhang, Y. Yang, D. Ren, L. Wang, X. He, Graphite as anode materials: Fundamental mechanism, recent progress and advances, Energy Storage Materials 36 (2021) 147-170. https://doi.org/10.1016/j.ensm.2020.12.027

[7] S. Afyon, F. Krumeich, C. Mensing, New High Capacity Cathode Materials for Rechargeable Li-ion Batteries: Vanadate-Borate Glasses, Sci Rep. 4 (2014) 7113. https://doi.org/10.1038/srep07113

[8] K. Feng, F. Wang, X. Yang, H. Zhang, X. Li, H. Zhang, LiCr(MoO4)2: a new high specific capacity cathode material for lithium ion batteries, J. Mater. Chem. A, 7(2) (2019) 567-573.N Doi:10.1039/C8TA10274K",

[9] S. Fang, D. Bresser, S. Passerini, Transition Metal Oxide Anodes for Electrochemical Energy Storage in Lithium- and Sodium-Ion Batteries, Adv. Energy Mater. 10 (2020) 1902485. https://doi.org/10.1002/aenm.201902485

[10] S. Lee, A. Manthiram, Can Cobalt Be Eliminated from Lithium-Ion Batteries? ACS Energy Letters 7(9) (2022) 3058-3063. DOI: 10.1021/acsenergylett.2c01553

[11] W. Jae, J. Song, J. J. Hong, J. Kim, Raspberry-like hollow Ni/NiO nanospheres anchored on graphitic carbon sheets as anode material for lithium-ion batteries, Journal of Alloys and Compounds, 805 (2019) 957-966. https://doi.org/10.1016/j.jallcom.2019.07.192.

[12] G. Zhu, L. Wang, H. Lin, L. Ma, P. Zhao, Y. Hu, T. Chen, R. Chen, Y. Wang, Z. Tie, J. Liu, Z. Jin, Walnut-Like Multicore–Shell MnO Encapsulated Nitrogen-Rich Carbon Nanocapsules as Anode Material for Long-Cycling and Soft-Packed Lithium-Ion Batteries, Adv. Funct. Mater. 28 (2018) 1800003. https://doi.org/10.1002/adfm.201800003

[13] Y. Lu, L. Yu, X. W. D. Lou, Nanostructured Conversion-type Anode Materials for Advanced Lithium-Ion Batteries, Chem 4(5) (2018) 972-996. https://doi.org/10.1016/j.chempr.2018.01.003.

[14] E. Kamali-Heidari, A. Kamyabi-Gol, Synthesis of mesoporous nickel iron oxide as a new anode material for high performance lithium ion batteries, Physica B: Condensed Matter 570 (2019) 176-181. https://doi.org/10.1016/j.physb.2019.06.023.

[15] R. U. Praveenkumar, S. Vivek, Clays: An Encouraging Catalytic Support, Current Catalysis 5(3) (2016). https://dx.doi.org/10.2174/2211544705666160624082343

[16] M. Belghazdis, E. K. Hachem, Clay and Clay Minerals: A Detailed Review, International Journal of Recent Technology and Applied Science 4(2) (2022) 54-75.

[17] F. Macht, K. Eusterhues, G. J. Pronk, K. U. Totsche, Specific surface area of clay minerals: Comparison between atomic force microscopy measurements and bulk-gas (N2) and -liquid (EGME) adsorption methods, Applied Clay Science 53(1) (2011) 20-26. https://doi.org/10.1016/j.clay.2011.04.006.

[18] A. Rodríguez, L. Fernández, J. R. Domínguez, G. González, O. Martínez, P. Espinoza-Montero, Mg and Ni nano-hydrotalcites modified with gold nanoparticles as platform of enzymatic electrochemical sensors for H_2O_2 detection, Sensing and Bio-Sensing Research 33 (2021) 100446. https://doi.org/10.1016/j.sbsr.2021.100446.

[19] X. Liu, G. Yang, Mechanisms for cation exchange at the interfaces of montmorillonite nanoparticles: Insights for Pb^{2+} control, Colloids and Surfaces A: Physicochemical and Engineering Aspects 641 (2022) 128556. https://doi.org/10.1016/j.colsurfa.2022.128556.

[20] L. C. Hsu, Y. M. Tzou, P. N. Chiang, W. M. Fu, M. K. Wang, H. Y. Teah, Y. T. Liu, Adsorption mechanisms of chromate and phosphate on hydrotalcite: A combination of macroscopic and spectroscopic studies, Environmental Pollution 247 (2019) 180-187. https://doi.org/10.1016/j.envpol.2019.01.012.

[21] M. Abbas, U. Sikander, M. T. Mehran, S. H. Kim, Exceptional stability of hydrotalcite derived spinel Mg(Ni)Al2O4 catalyst for dry reforming of methane, Catalysis Today 403 (2022) 74-85. https://doi.org/10.1016/j.cattod.2021.08.029.

[22] S. Miyata, Anion-exchange properties of hydrotalcite-like compounds, Clays and Clay Minerals 31 (1983) 305–311. https://doi.org/10.1346/CCMN.1983.0310409

[23] L. Zhirong, Md. Azhar Uddin, S. Zhanxue, FT-IR and XRD analysis of natural Na-bentonite and Cu(II)-loaded Na-bentonite, Spectrochimica Acta Part A: Molecular and Biomolecular Spectroscopy 79(5) (2011) 1013-1016. https://doi.org/10.1016/j.saa.2011.04.013.

[24] Y. Shitong, J. Li, Y. Lu, Y. Chen, X. Wang, Sorption of Ni(II) on GMZ bentonite: effects of pH, ionic strength, foreign ions, humic acid and temperature, Applied radiation and isotopes 67(9) (2009) 1600-1608. https://doi.org/10.1016/j.apradiso.2009.03.118

[25] S. Bandipally, C. Cherian, D. N. Arnepalli, Characterization of Lime-Treated Bentonite Using Thermogravimetric Analysis for Assessing its Short-Term Strength Behaviour, Indian Geotechnical Journal 48 (2018) 393–404. https://doi.org/10.1007/s40098-018-0305-7

[26] K. K. Norrfors, M. Bouby, S. Heck, N. Finck, R. Marsac, Montmorillonite colloids: I. Characterization and stability of dispersions with different size fractions, Applied Clay Science 114 (2015) 179 - 189. 10.1016/j.clay.2015.05.028.

[27] L. Fernández, C. Borrás, H. Carrero, Electrochemical behavior of phenol in alkaline media at hydrotalcite-like clay/anionic surfactants/glassy carbon modified electrode, Electrochim. Acta. 52 (2006) 872–884. https://doi.org/10.1016/j.electacta.2006.06.021

[28] G. S. Macala, A. W. Robertson, C. L. Johnson, Z. B. Day, R. S. Lewis, M. G. White, A. V. Iretskii, P. C. Ford, Transesterification Catalysts from Iron Doped Hydrotalcite-like Precursors: Solid Bases for Biodiesel Production. Catal Lett. 122 (2008) 205–209. https://doi.org/10.1007/s10562-008-9480-y

[29] N. kulianti, T. Wardani, I. Gunardi, A. Roesyadi, Effect of Calcination at Synthesis of Mg-Al Hydrotalcite Using co-Precipitation Method, The Journal of Pure and Applied Chemistry Research 6(1) (2017) 7-13. doi:http://dx.doi.org/10.21776/ub.jpacr.2017.006.01.280

[30] S. Abelló, E. Bolshak, D. Montané, Ni–Fe catalysts derived from hydrotalcite-like precursors for hydrogen production by ethanol steam reforming, Applied Catalysis A: General 450 (2013) 261-274. https://doi.org/10.1016/j.apcata.2012.10.035.

[31] R. W. Cairns, Emil Ott, X-Ray Studies of the System Nickel—Oxygen—Water. I. Nickelous Oxide and Hydroxide, J. Am. Chem. Soc. 55(2) (1933) 527–533. https://doi.org/10.1021/ja01329a013

[32] P. Dubey, N. Kaurav, R. S. Devan G. S. Okram Y. K. Kuod, The effect of stoichiometry on the structural, thermal and electronic properties of thermally decomposed nickel oxide, RSC Adv. 8 (2018) 5882-5890. https://doi.org/10.1039/C8RA00157J

[33] Y. Serna Morales, J. Guateque, Y. P. Ávila Torres, Recuperación de Hidrocarburos a partir de residuos de polietileno de baja densidad, Inf. Téc. 80(2) (2016) 121-127. ISSN 0122-056X, ISSN-e 2256-5035

[34] H. A. Patel, R. S. Somani, H. C. Bajaj, et al. Nanoclays for polymer nanocomposites, paints, inks, greases and cosmetics formulations, drug delivery vehicle and waste water treatment, Bull Mater Sci 29 (2006) 133–145. https://doi.org/10.1007/BF02704606

[35] A. A. Tireli, R. Guimarães Ido, J. C. Terra, R. R. da Silva, M. C. Guerreiro, Fenton-like processes and adsorption using iron oxide-pillared clay with magnetic properties for organic compound mitigation, Environ Sci Pollut Res Int. 22(2) (2015) 870-81. doi: 10.1007/s11356-014-2973-x.

[36] M. A. Kafi, A. Sadeghi-Nik, A. Bahari, A. Sadeghi-Nik, E. Mirshafiei, Microstructural Characterization and Mechanical Properties of Cementitious Mortar Containing Montmorillonite Nanoparticles, Journal of Materials in Civil Engineering 28(12) (2016) 04016155. doi:10.1061/(ASCE)MT.1943-5533.0001671.

[37] A. Rodrigues, A. Brito, P. Janknecht, M. F. Proença, R. Nogueira, Quantification of humic acids in surface water: effects of divalent cations, pH, and filtration, J. Environ. Monit. 11(2) (2009) 377-382 DOI: 10.1039/B811942B

[38] L. P. Figueredo Benício, R. Alvarenga Silva, J. Aparecida Lopes, D. Eulálio, R. M. Menezes dos Santos, L. Angelo de Aquino, L. Vergütz, R. Ferreira Novais, L. M. da Costa, F. Garcia Pinto, J. Tronto, LAYERED DOUBLE HYDROXIDES: NANOMATERIALS FOR APPLICATIONS IN AGRICULTURE, R. Bras. Ci. Solo 39 (2015) 1-13. https://doi.org/10.1590/01000683rbcs2015081

[39] K. Shekoohi, F. S. Hosseini, A. H. Haghighi, A. Sahrayian, Synthesis of some Mg/Co-Al type nano hydrotalcites and characterization, MethodsX 4 (2017) 86-94. https://doi.org/10.1016/j.mex.2017.01.003.

[40] R. S. Hebbar, A. M. Isloor, B. Prabhu, Inamuddin, M. A. Asiri, A. F. Ismail, Removal of metal ions and humic acids through polyetherimide membrane with grafted bentonite clay, Sci Rep. 8 (2018) 4665. https://doi.org/10.1038/s41598-018-22837-1

[41] Z. Zhou, W. Zhang, T. Yu, Y. Li, A. Struhárová, M. Matejdes, M. Slaný, G. Chen, The Effect of Sodium Bentonite in the Thermo-Catalytic Reduction of Viscosity of Heavy Oils, Molecules 28 (2023) 2651. https://doi.org/10.3390/molecules28062651

[42] E. E. I. Elkhalifah, S. Maitra, M. Azmi Bustam, T. Murugesan. Thermogravimetric analysis of different molar mass ammonium cations intercalated different cationic forms of montmorillonite. J Therm Anal Calorim. 110 (2012) 765–771.

[43] Z. Abdelsadek, J. P. Holgado, D. Halliche, Examination of the Deactivation Cycle of NiAl- and NiMgAl-Hydrotalcite Derived Catalysts in the Dry Reforming of Methane, Catal Lett. 151 (2021) 2696–2715. https://doi.org/10.1007/s10562-020-03513-4

[44] Z. B. Quchan Atigh, A. Heidari, A. Karimi, M. A. Pezhman, B. A. Lajayer, E. C. Lima, Purification and economic analysis of nanoclay from bentonite, Environmental Science and Pollution Research 28 (2021) 13690–13696. doi:10.1007/s11356-020-11595-1

[45] J. Y. Juang Yeo, D. S. Khaerudini, F. E. Soetaredjo, G. L. Waworuntu, S. Ismadji, A. Putranto, J. Sunarso, Experimental and modelling study of adsorption isotherms of amoxicillin, ampicillin and doripenem on bentonite-chitosan composite, South African Journal of Chemical Engineering Volume 43 (2023) 38-45. https://doi.org/10.1016/j.sajce.2022.09.013.

[46] M. El Miz, H. Akichoh, D. Berraaouan, S. Salhi, A. Tahani, Chemical and Physical Characterization of Moroccan Bentonite Taken from Nador (North of Morocco), American Journal of Chemistry 7(4) (2017) 105-112.

[47] N. Tien Thao, D. V. Long, D. M. Hogan, Conversion of styrene into benzaldehyde and styrene epoxide over MgCoAl-LDH catalysts, Vietnam J. Sci. Technol. 55(4) (2017) 403–410. https://doi.org/10.15625/2525-2518/55/4/8510

[48] M. Önal, Y. Sarıkaya, Thermal behavior of a bentonite. J Therm Anal Calorim. 90 (2007) 167–172. https://doi.org/10.1007/s10973-005-7799-9

[49] G. K. Bhattacharyya, S. Sen Gupta, Kaolinite and montmorillonite as adsorbents for Fe(III), Co(II) and Ni(II) in aqueous medium, Applied Clay Science 41(1-2) (2008) 1-9. https://doi.org/10.1016/j.clay.2007.09.005.

[50] J. Sanz, J. I. Lombraña, A. M. De Luis, M. Ortueta, F. Varona, Microwave and Fenton's reagent oxidation of wastewater, Environ Chem Lett 1 (2003) 45–50. https://doi.org/10.1007/s10311-002-0007-2

[51] A. Habib, S. Serniabad, M. S. Khan, R. Islam, M. Chakraborty, A. Nargis, M. E. Quayum, M. A. Alam, V. Rapozzi, M. Tabata, Formation of Nickel(II)Porphyrin and Its Interaction with DNA in Aqueous Medium, Preprints.org (2021) 2021010434. https://doi.org/10.20944/preprints202101.0434.v1

[52] E. Wieland, H. Wanner., Y. Albinsson, P. Wersin, O. Karnland, A surface chemical model of the bentonite-water interface and its implications for modelling the near field chemistry in a repository for spent fuel, SKB Technical Reports 94-26 (1994) https://www.skb.com/publication/10581

[53] S. K. Isalou, M. Ghorbanpour, Catalytic activity of Fe-modified bentonite in heterogeneous photo-Fenton process, Desalination and Water Treatment 162 (2019) 376-382.

[54] J.de Carvalho Arjona, M. das Graças Silva-Valenzuela, S. H. Wang, F. R. Valenzuela-Diaz, Biodegradable Nanocomposite Microcapsules for Controlled Release of Urea, Polymers 13 (2021) 722. https://doi.org/10.3390/polym13050722.

[55] M. A. Rehman, T. Jafri, Stabilization of low plastic and high plastic clay using guar gum biopolymer, Journal of Applied Research on Industrial Engineering 7(4) (2020) 329-343. doi: 10.22105/jarie.2020.247859.1195

[56] H. Y. Zeng, Y. J. Wang, Z. Feng, K. Y. You, C. Zhao, J. W. Sun, P. L. Liu, Synthesis of Propylene Glycol Monomethyl Ether Over Mg/Al Hydrotalcite Catalyst, Catal Lett. 137 (2010) 94–103. https://doi.org/10.1007/s10562-010-0335-y

[57] P. Keil, A. Jossen, Charging protocols for lithium-ion batteries and their impact on cycle life—An experimental study with different 18650 high-power cells, Journal of Energy Storage 6 (2016) 125-141. https://doi.org/10.1016/j.est.2016.02.005.

[58] S. P. Guo, Z. Ma, J. C. Li, H. G. Xue, First investigation of the electrochemical performance of γ-LiFeO2 micro-cubes as promising anode material for lithium-ion batteries, J Mater Sci. 52 (2017) 1469–1476. https://doi.org/10.1007/s10853-016-0441-3

[59] W. Xinghui, L. Xiuwan, S. Xiaolei, L. Fei, L. Qiming, W. Qi, H. Deyan, Nanostructured NiO electrode for high rate Li-ion batteries, J. Mater. Chem. 21(11) (2011) 3571-3573. 10.1039/C0JM04356G

[60] C. Shen, G. Hu, L. Z. Cheong, S. Huang, J. G. Zhang, D. Wang, Direct Observation of the Growth of Lithium Dendrites on Graphite Anodes by Operando EC-AFM, Small Methods 2 (2018) 1700298. https://doi.org/10.1002/smtd.201700298

[61] L. Shuai, Z. Xiaojie, L. Dongqing, W. Shuwei, Z. Lihan, Z. Rui, K. Feiyu, L. Baohua, Understanding the Conductive Carbon Additive on Electrode/Electrolyte Interface Formation in Lithium-Ion Batteries via in situ Scanning Electrochemical Microscopy, Frontiers in Chemistry 8 (2020) 114. 10.3389/fchem.2020.00114

[62] L. Hao, W. Guoxiu, L. Jian, Q. Shizhang, A. Hyojun, Highly ordered mesoporous NiO anode material for lithium ion batteries with an excellent electrochemical performance, J. Mater. Chem. 21(9) (2011) 3046-3052. 10.1039/C0JM03132A

[63] C. Zhang, N. Qin, A. Pan, J. Yuan, Q. Liu, J. Ren, Z. h. Xue, M. Iqbal, Y. Tian & F. Ke, Hollow Fe2O3 nanotubes derived from metal-organic framework for enhanced lithium storage and dye adsorption, J Porous Mater, 28 (2021) 673–681. https://doi.org/10.1007/s10934-020-01019-3

[64] T. Mu, Y. Zhao, C. Zhao, N. Graham Holmes, S. Lou, J. Li, W. Li, M. He, Y. Sun, C. Du, R. Li, J. Wang, G. Yin, X. Sun, Stable Silicon Anodes by Molecular Layer Deposited Artificial Zincone Coatings, Adv. Funct. Mater. 31 (2021) 2010526. https://doi.org/10.1002/adfm.202010526.

[65] J. Hwang, D. Yadav, H. Yang, I. Jeon, D. Yang, J. W. Seo, M. Kang, S. Y. Jeong, C. R. Cho C-R, In Situ Electrochemical Impedance Measurements of α-Fe2O3 Nanofibers: Unravelling the Li-Ion Conduction Mechanism in Li-Ion Batteries, Batteries 8(5) (2022) 44. https://doi.org/10.3390/batteries8050044

[66] M. G. Ortiz, A. Visintin, S. G. Real, Synthesis and electrochemical properties of nickel oxide as anodes for lithium-ion batteries, Journal of Electroanalytical Chemistry 883 (2021) 114875. https://doi.org/10.1016/j.jelechem.2020.114875.

[67] R. Qilong, W. Guangyu, X. Weinan, H. Jiangang, L. Pingping, L. Bo, C. Junye, W. Shuilin, Z. Rujia, H. Junqing, Highly Ordered Mesoporous NiCo2O4 as a High Performance Anode Material for Li-Ion Batteries, Frontiers in Chemistry 7 (2019) 521. 10.3389/fchem.2019.00521.

List of figures

Fig. 14. Charge and discharge profiles at selected cycles for HT2NC-400 (a) and HT-400 (b) electrodes (insert in (a): cyclic voltammetry of a Natural clay (NC) and conductive super P Carbon, 3.0-0.01 V, 0.1 mV s^{-1}).

Fig. 15. Cyclic voltammograms for both materials at 0.1 mV s^{-1} and (3.0 -0.01 V) during first (a) and second cycle (b).

Fig. 16. Cyclic voltammograms for both materials at 0.1 mV s^{-1} and (3.0 -0.01 V) during 200 cycles (insert: discharge capacity values are presented for the electrodes close to the 200 cycles).

Fig. 17. Nyquist plots, (insert: high frequency region and equivalent circuit) (a), Z_R vs $\omega^{-0.5}$ (b) of the electrodes at 50% SOC after 200 galvanostatic cycles.

Fig. 18. Rate capability for HT-400 and HT2NC-400 electrodes.

Figures

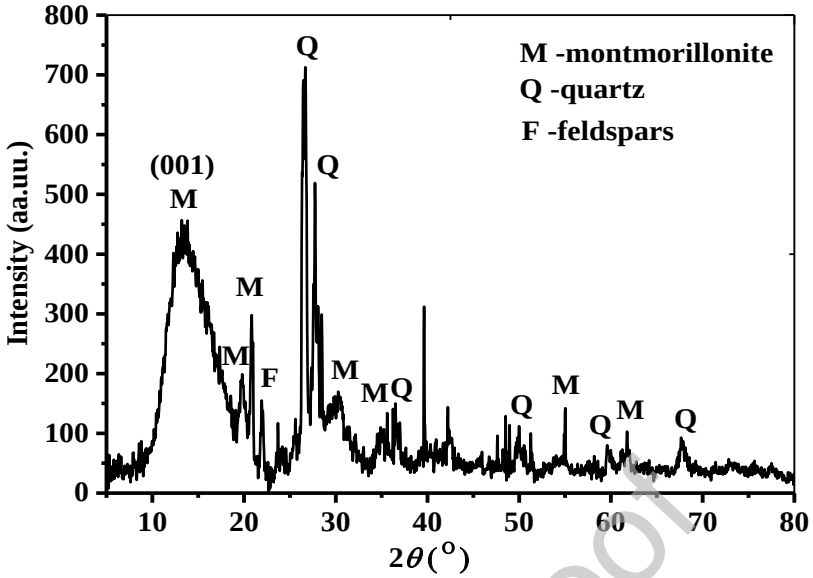

Fig. 1

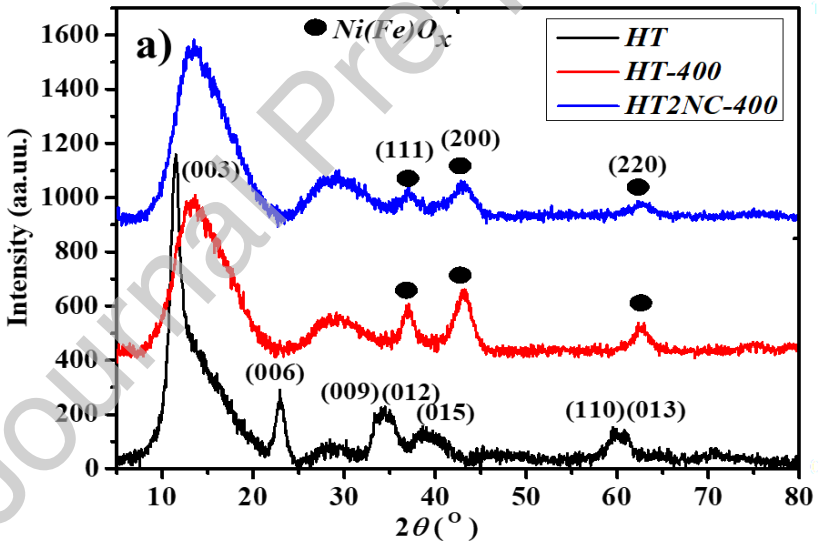

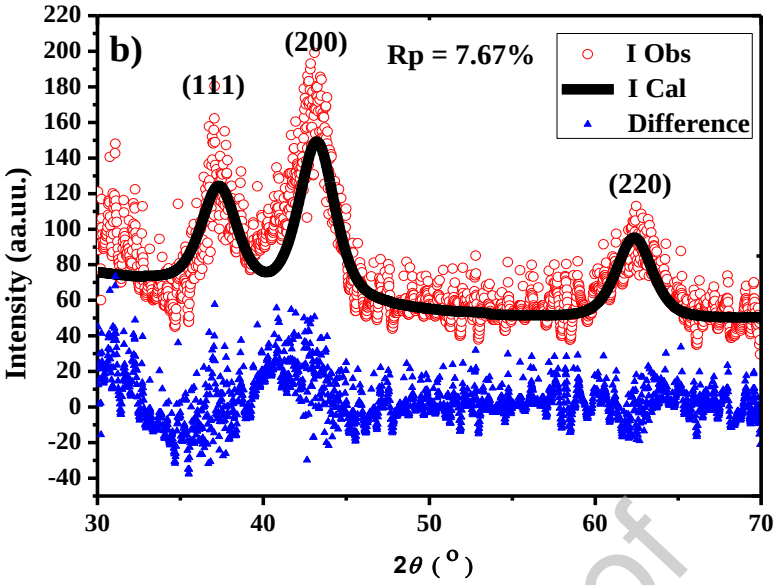

Fig. 2

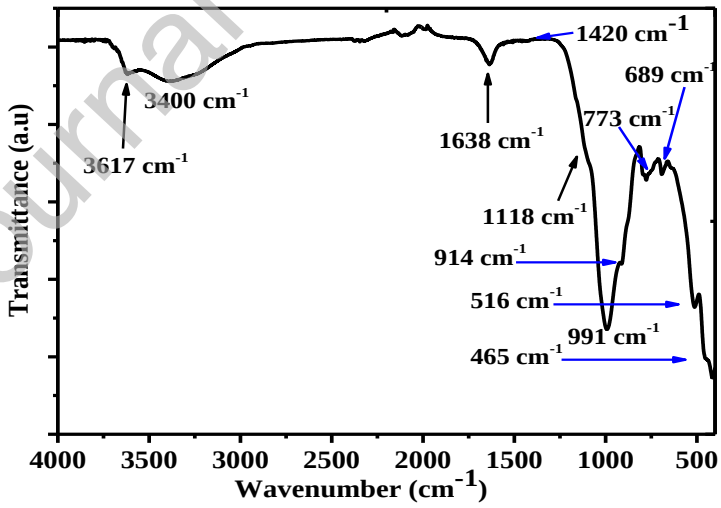

Fig. 3

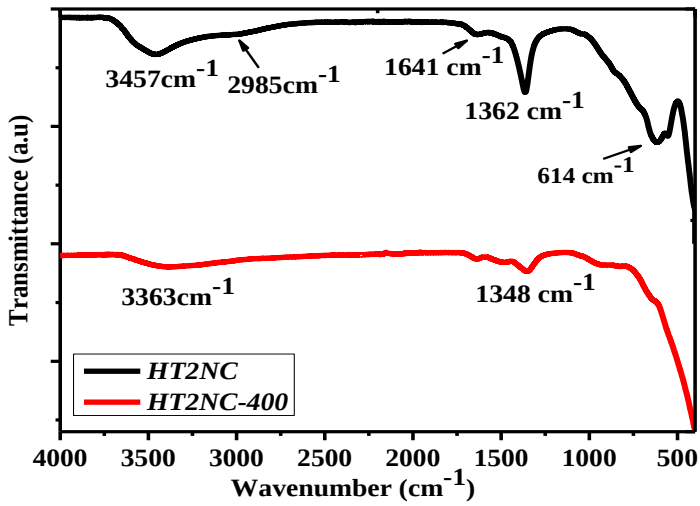

Fig. 4

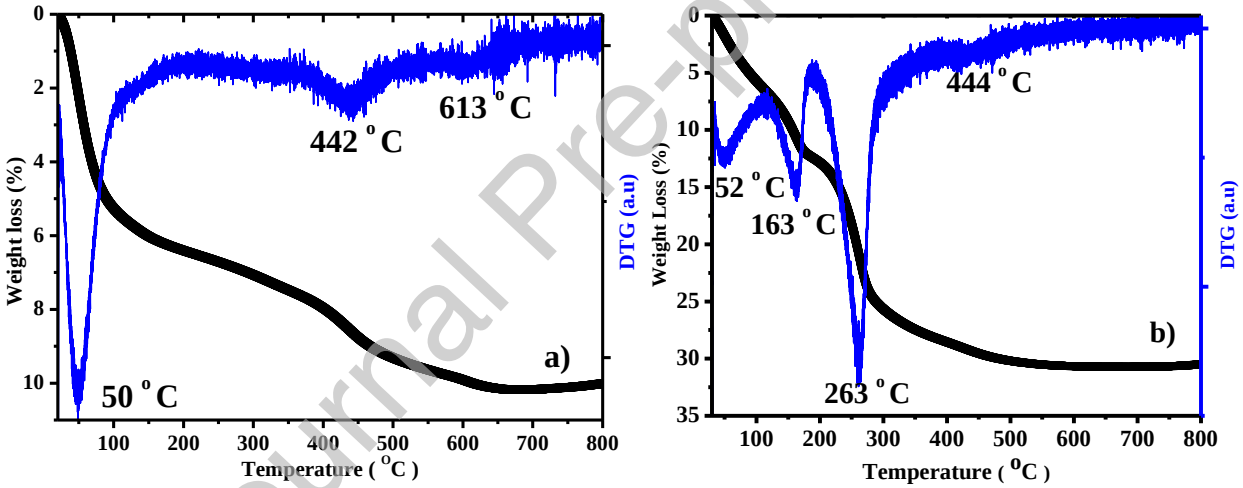

Fig. 5

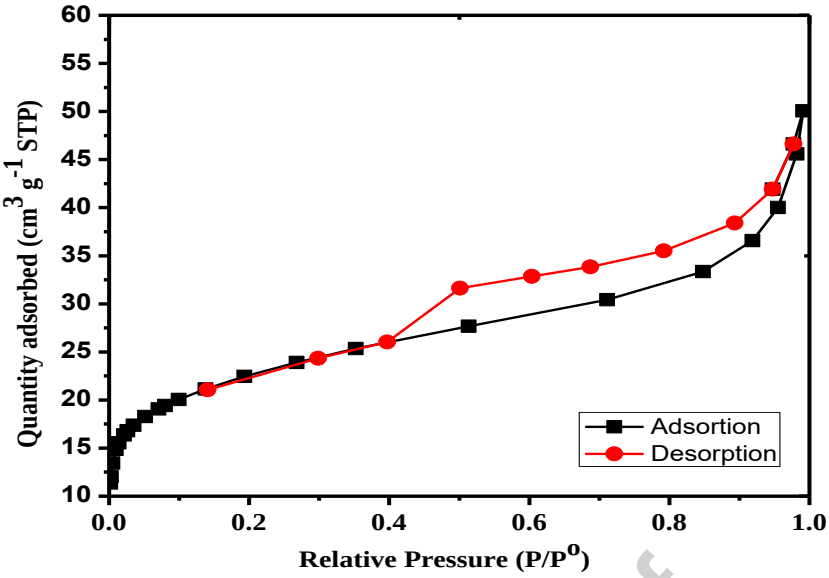

Fig. 6

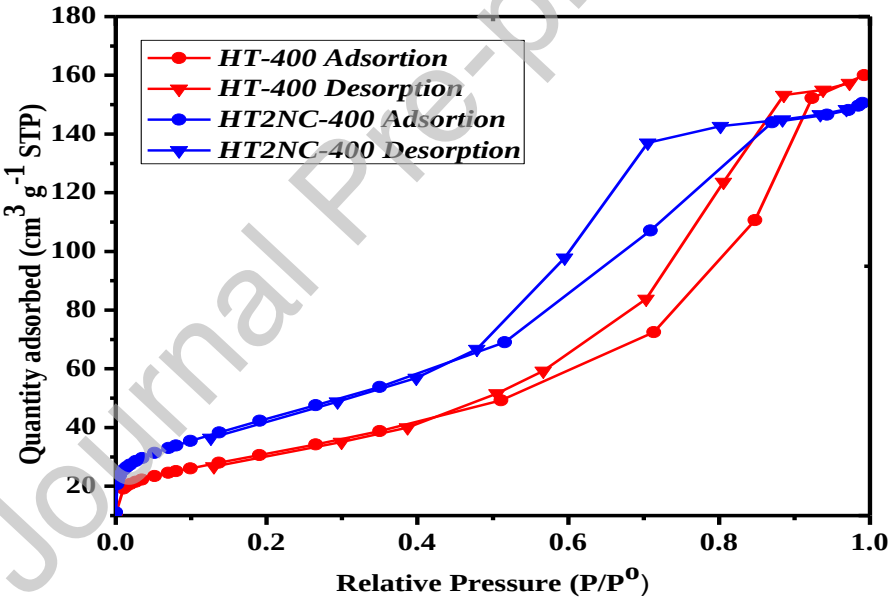

Fig. 7

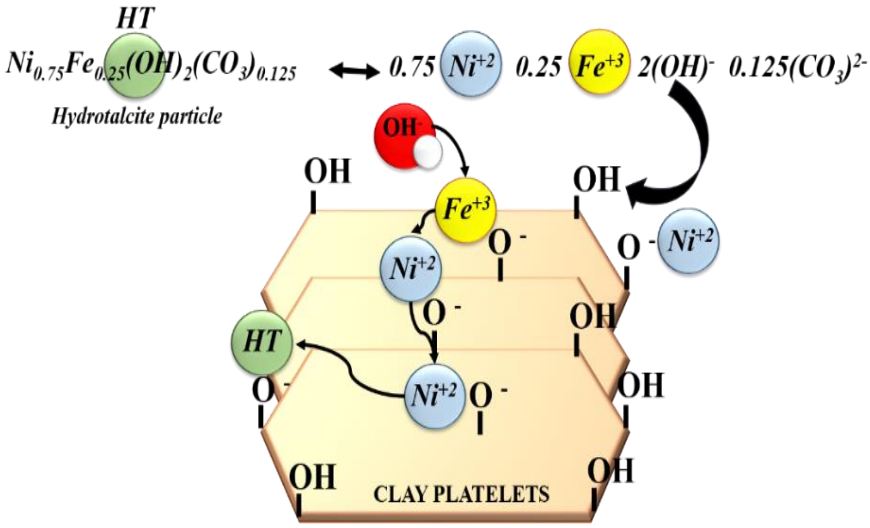

Fig. 8

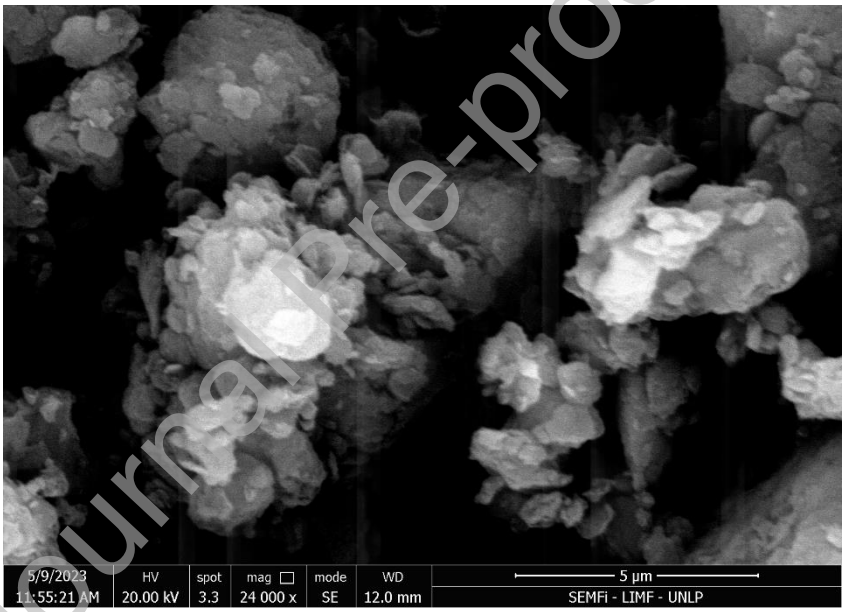

Fig. 9

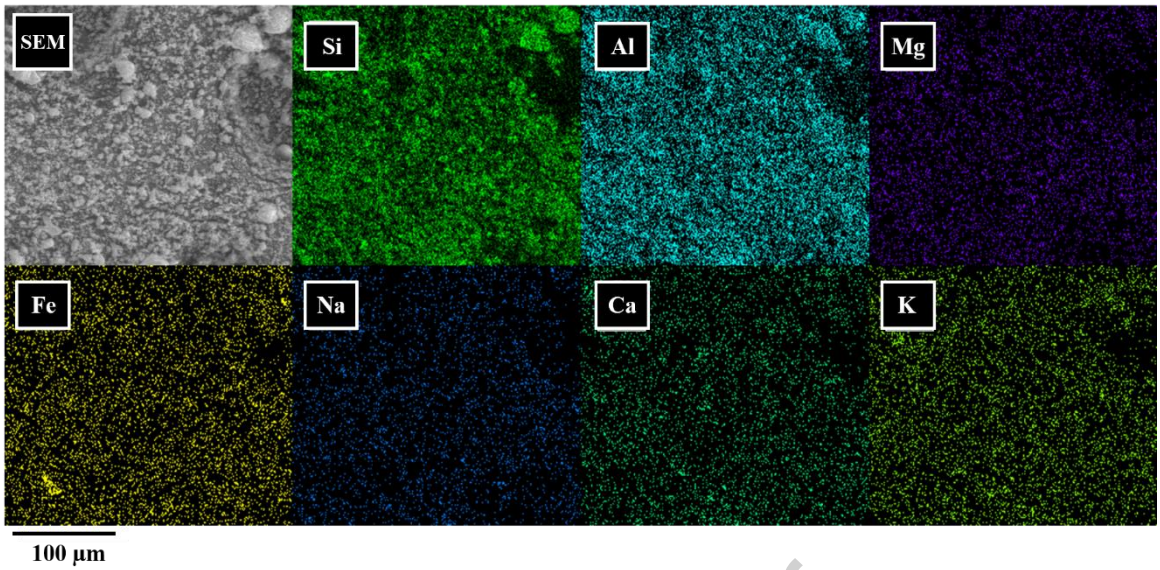

Fig. 10

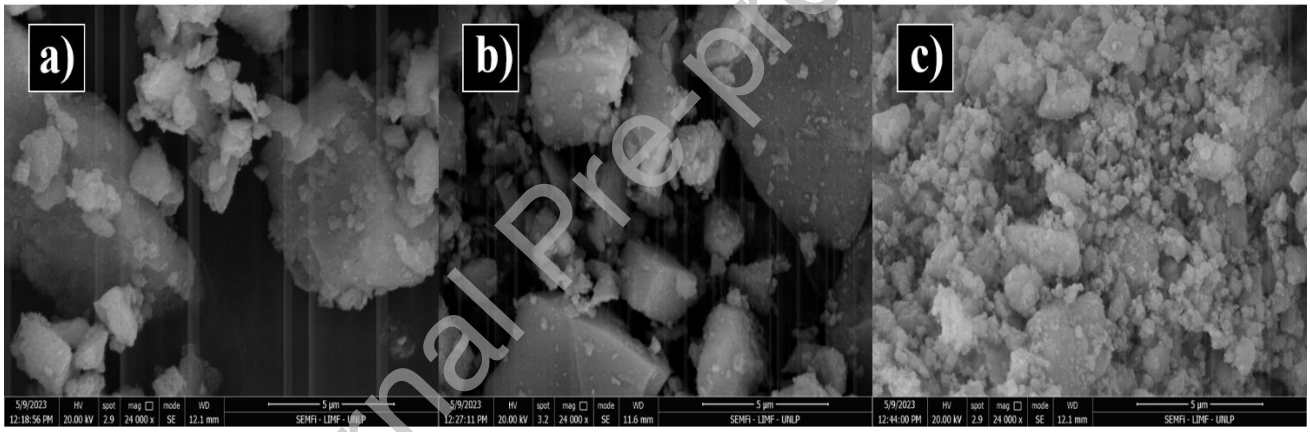

Fig. 11

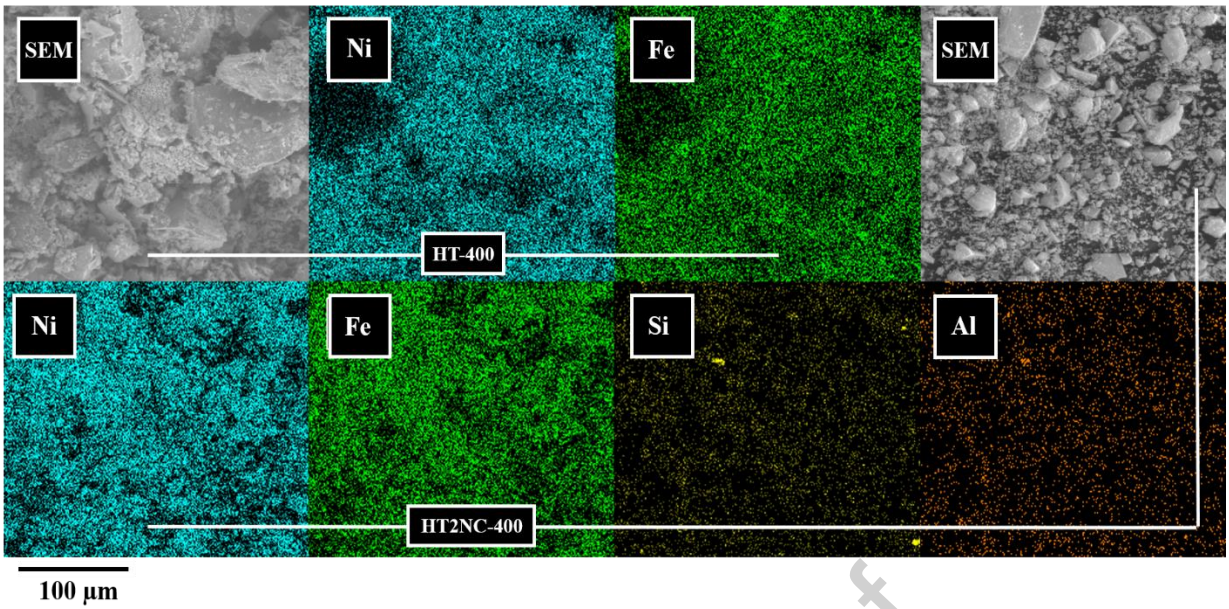

Fig. 12

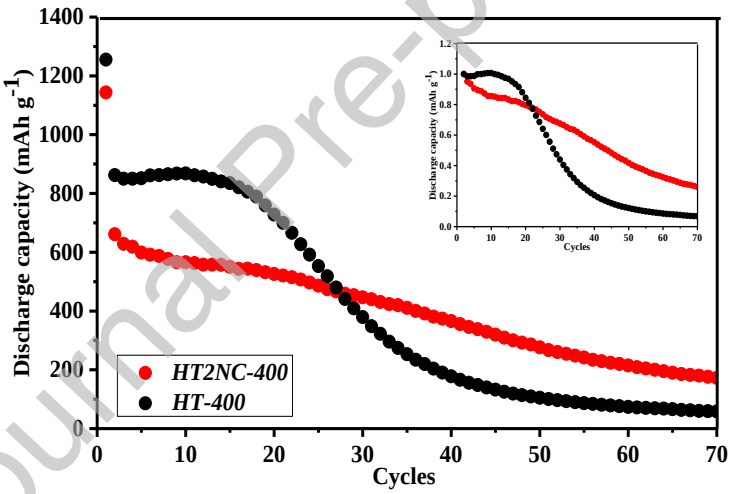

Fig. 13

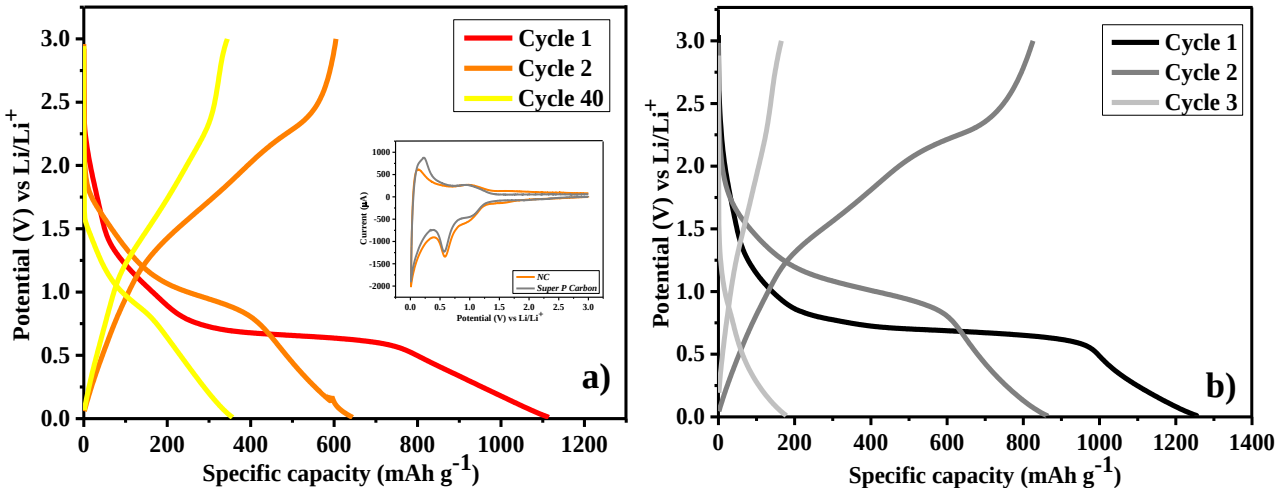

Fig. 14

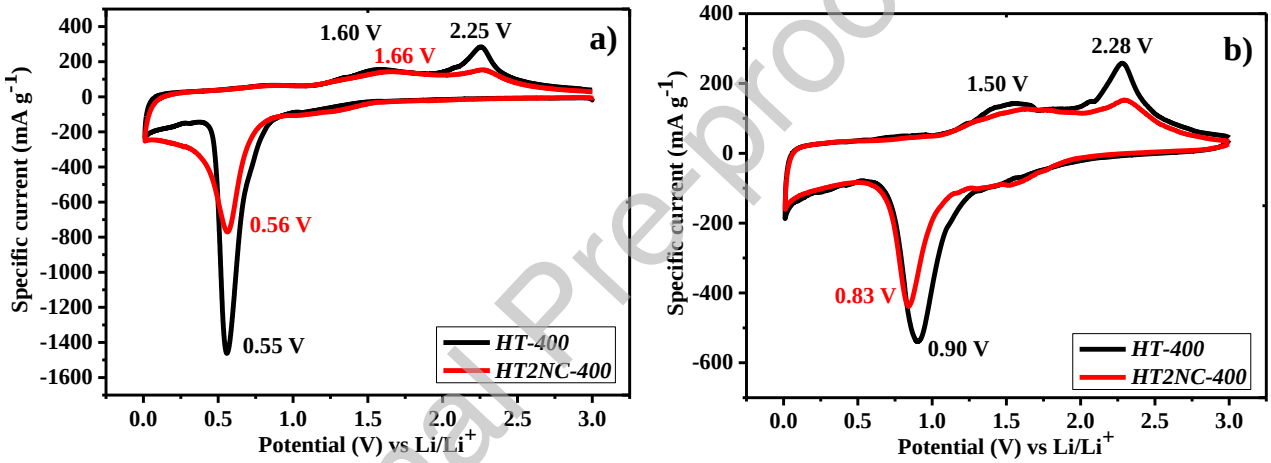

Fig. 15

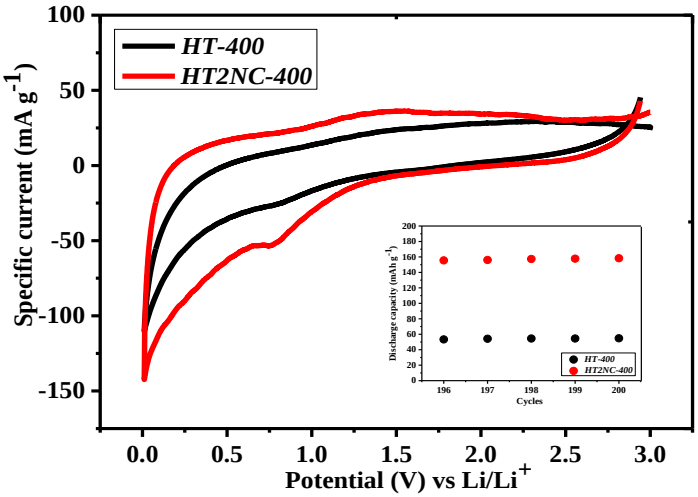

Fig. 16

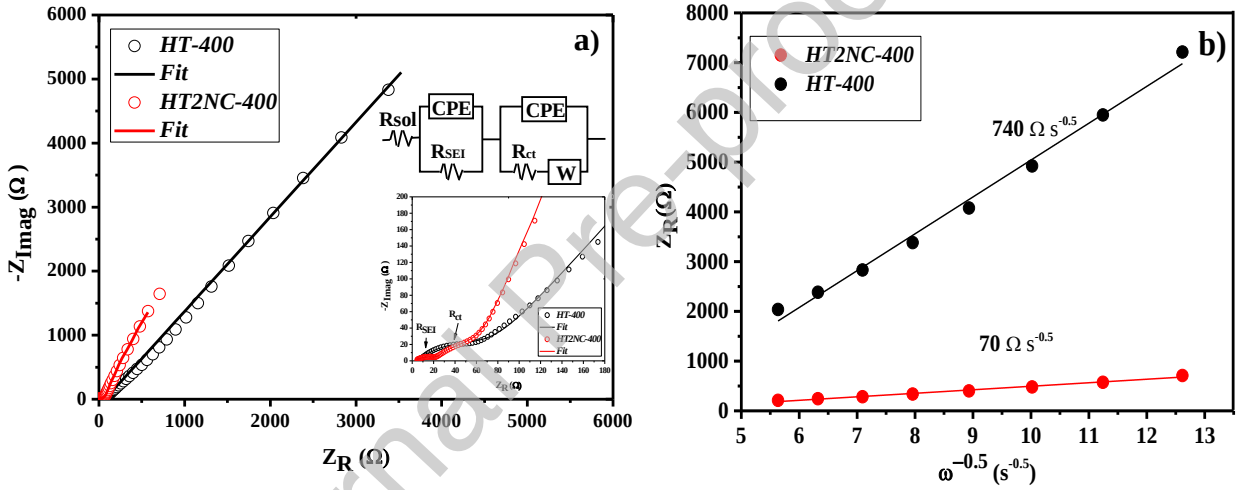

Fig. 17

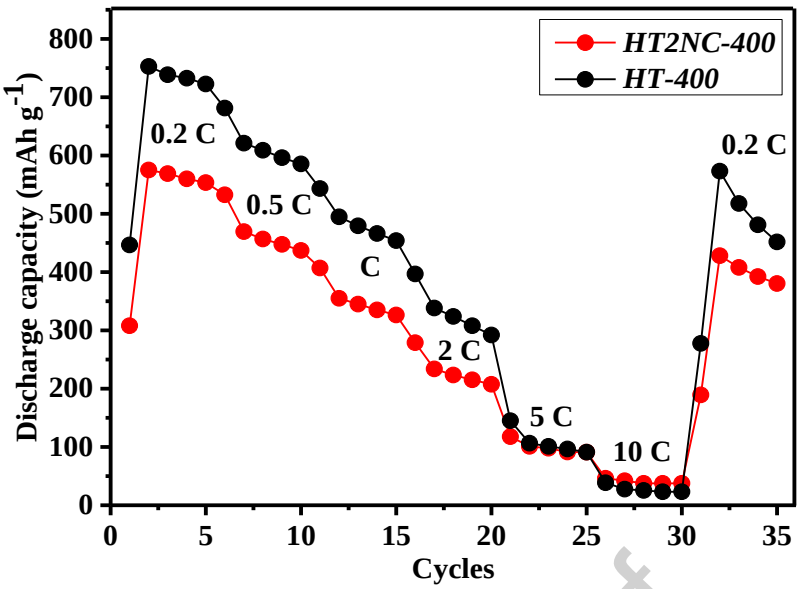

Fig. 18

Declaration of interests

☐ The authors declare that they have no known competing financial interests or personal relationships that could have appeared to influence the work reported in this paper.

☒ The authors declare the following financial interests/personal relationships which may be considered as potential competing interests:

Augusto Rodriguez reports financial support was provided by Consejo Nacional de Investigaciones Científicas y Técnicas (CONICET). Augusto Rodriguez reports financial support was provided by Agencia Nacional de Promoción Científica y Tecnológica (ANPCyT). Augusto Rodriguez reports a relationship with Agencia Nacional de Promoción Científica y Tecnológica (ANPCyT) that includes: funding grants.